SIMULATION AND ANALYSIS OF BEARING PAD TO PRESSURE TUBE CONTACT HEAT TRANSFER UNDER LARGE BREAK LOCA CONDITIONS

M.H. BAYOUMI, W.C. MUIR and P.B. MIDDLETON

Ontario Hydro, Reactor Safety and Operational Analysis Department
700 University Avenue, Toronto, Ontario, M5G-1X6

ABSTRACT

In some postulated loss-of-coolant accidents (LOCAs) in a CANDU reactor, localized "hot spots" can develop on the pressure tube as a result of decay heat dissipation by conduction through bearing pad/pressure tube contact locations. Depending on the severity of flow degradation in the channel, these "hot spots" could represent a potential threat to fuel channel integrity. The most important parameter in the simulation of BP/PT contact is the contact conductance. Since BP/PT thermal contact conductance is a complex parameter which depends upon the thermal and physical characteristics of the material junction and the surrounding environment, contact conductance is determined from experiments relevant to the reactor conditions.

A series of twelve full scale integrated BP/PT contact experiments have been conducted at AECL-WRL under Candu Owner Group (COG). The objective of the experiments was to investigate the effect of BP/PT contact on PT thermal-mechanical behaviour. This paper presents the simulation of the BP/PT interaction integrated experiments using SMARTT and MINI-SMARTT computer codes and subsequent derivation of the BP/PT contact conductance by best fitting of the experimental pressure tube temperature measurements.

INTRODUCTION

In a number of postulated Loss-of-Coolant Accidents (LOCAs), some of the fuel channels in a CANDU reactor are predicted to initially experience periods of very low flow. The coolant could boil off completely and the pressure tube become dry in a few seconds as flow stagnation occurs. The circumference of the pressure tube will be heated by thermal radiation except at locations where the bearing pads are in contact with the pressure tube. At the bearing pad locations, conduction is the dominant heat transfer mechanism. As a result, hot regions can potentially develop on the pressure tube circumference under the bearing pads. Depending on the thermalhydraulic transient experienced due to a large break LOCA, the pressure tube could potentially rupture before ballooning into contact with the calandria tube.

An experimental program, "Bearing Pad/Pressure Tube Interaction", has been carried out at WRL under COG. The objective of this program is to study the influence of hot bearing pads on the pressure tube temperature transient and the consequence of mechanical deformation during an accident such as a large break LOCA. The experimental data is used to derive the contact conductance values between the bearing pad and the pressure tube. The derived contact conductance value is used in the validation of computer codes and in the analysis of CANDU reactors.

The test program was divided into two phases. The first phase consisted of four experiments that used superheated steam as the pressurizing medium. In all of the four experiments in this series, the pressure tube ballooned into contact with the calandria tube. In these experiments, steam condensed on the water-cooled end fitting and re-entered the bottom of the pressure tube at the ends of the relatively short section. The evaporation of this condensed water created non-representative temperature gradients on the pressure tube and the fuel element simulator (FES) bundle.

The second phase, which consisted of eight experiments, used a gas mixture of 75% Ar-25% O_2 (simulated steam) as the pressurizing medium to avoid the condensation problem experienced in the first phase. Three pressure tube failures occurred in this series. Two pressure tubes ruptured at a pressure of 6 MPa due to large circumferential differential temperatures (experiments 6 and 10). The third pressure tube failure occurred in experiment 12 due to fuel element contact with the pressure tube between bearing pad rings during ballooning of the pressure tube.

Analysis of these integrated experiments was initiated to derive BP/PT contact conductance values which are most likely to represent the conditions prevailing in a full scale CANDU channel. Both the SMARTT [1] and MINI-SMARTT [2] computer codes were used in these analyses. The SMARTT code was used to generate the thermodynamic transients which were used as input to the MINI-SMARTT computer code. The MINI-SMARTT code was used to derive the BP/PT contact conductance by best fitting the experimentally measured transient pressure tube temperatures. MINI-SMARTT is flexible and capable of simulating multiple bearing pads contacting the pressure tube at any circumferential location. Multiple BP/PT contact capabilities have been introduced into the code to simulate a bundle under axial constrained expansion where some fuel elements may slightly bend causing the bearing pads to contact the pressure tube at different locations around the pressure tube circumference.

The objective of this paper is to discuss the simulation methodology of BP/PT contact and present the simulation results and the derived values for BP/PT contact conductance. Also, the results of a parametric study are presented to examine the sensitivity of the results to different parameters such as pressure tube and sheath emissivities. A complete analysis and discussion of the results are provided in the paper. Recommendations are made as to what appropriate BP/PT contact conductance should be used in CANDU reactor analysis.

EXPERIMENTAL APPARATUS

The experimental apparatus consisted of a 1.2 m long section of CANDU-typical autoclaved Zr-2.5Nb pressure tube mounted inside a 1.1 m long section of Zr-2 calandria tube (Figure 1). The pressure tube was connected to a blow down tank which served as a reservoir to help maintain pressure during the volume change which occurred during pressure tube ballooning. The pressure tube was surrounded by a calandria tube which in turn was surrounded by heated water in an open tank. The annulus between the pressure tube and calandria tube was purged with CO_2 prior to the start of the tests. The annulus was not a sealed system and its pressure remained essentially atmospheric throughout the tests.

Figure 2 shows a cross section of the electrically heated FES bundle configuration. The fuel element simulators are arranged to represent the outer ring of 16 fuel elements in a typical 28-element CANDU fuel bundle. Bearing and spacer pads were spot-welded to the FES sheaths in five axial rings. The five rings are shown via dashed lines inside the pressure tube in Figure 1. These rings are positioned at the FES axial centre as well as 197 mm and 394 mm on either side of the centre. The bearing pads are brazed on all 16 FESs at the central bearing pad ring to simulate typical 28-element CANDU fuel pins. Central tungsten weight cans were placed inside the ring of the FESs to make the mass per unit length of the FES bundle (~50 g/mm) similar to a 28-element CANDU fuel bundle. Zirconium wires were spot-welded to the stainless steel shell to support the weight cans on the FES cladding (Figure 2). These support wires in combination with insulation inside the shell, helped reduce heat losses from the FES bundle to the tungsten weights. Nine of these weight cans were positioned along the 1100 mm heated axial length of the test section.

Each fuel element simulator (FES) contained 99.7% minimum purity alumina (Al_2O_3) pellets which electrically insulated the cladding from the graphite rod heater filaments. The 6 mm diameter graphite rod heater filaments were plasma flame-spray coated with tungsten carbide to minimize the reaction between alumina and graphite at high temperatures. These graphite rod heaters had a heated length of 1100 mm.

INSTRUMENTATIONS

Voltage taps were placed on the power supply connectors to record the voltage drop across the various FESs. The power generated in the FES heater bundle circuit was calculated from the measured voltage drop across the voltage taps and current supplied from the power supply.

Three thermocouples were placed inside the bottom FES, 12 thermocouples were placed on the FES surfaces; 32 (30 in the first phase) thermocouples were on the outside surface of the pressure tube and 6 to 8 thermocouples were on the outside surface of the calandria tube. Cross sections through the test section show the location of various

thermocouples located at the test section centreline (Figure 3) and 98.4 mm from the centreline towards the exit end. Thermocouples and resistance temperature detectors (RTDs) were used to measure the temperature of the water in the tank surrounding the calandria tube.

Top and bottom displacement transducers consisting of Linear Variable Differential Transformers (LVTDs) located +6 mm off the test section centreline (Figure 1) are used to measure the relative displacement of the pressure tube with respect to the calandria tube. A third LVTD, located +104.4 mm from the centreline on the bottom of the test section, was added for Tests 8 and 12 to measure the pressure tube displacement (ballooning) between bearing pad rings. The entire test was recorded using video cameras to observe any nucleate or film boiling on the calandria tube. One camera was mounted above the test section and another was aimed through a lexan window in the side of the tank. A mirror was positioned inside the tank so that the side camera could record nucleate or film boiling on the bottom of the calandria tube. A third camera was used to record the overall view of the test apparatus during selected experiments.

EXPERIMENTAL CONDITIONS AND RESULTS

The test conditions and major experimental results for the first four experiments are listed in Table 1. In the first two tests, the coolant pressure was 3.0 MPa while in the third and fourth tests, the coolant pressure was 6.0 MPa. The experiments performed in the first phase had steam pressurization. In all four experiments, the pressure tube ballooned into contact with the calandria tube around the entire circumference and axially along the entire heated length. The FES with internal weight cans sagged as a unit such that the central bottom bearing pads remained in contact with the pressure tube during the ballooning process.

Table 2 lists the major test conditions and results of the eight experiments performed in the second phase that used simulated steam as the pressurizing medium. In all phase 2 experiments, the pressure tube ballooned into contact with the calandria tube around the entire circumference and axially along the heated length (except in Tests 6, 10 and 12 where the pressure tube ruptured). The pressure tube ruptured in Tests 6 and 10 due to a large top-to-bottom circumferential temperature differential at relatively high pressure (6 MPa). In Test 12, the pressure tube ruptured inside the calandria tube shortly after initial pressure tube/calandria tube contact. The rupture occurred on the bottom between bearing-pad rings and appeared to be caused by FES cladding contact with the pressure tube. The combination of high FES temperature, concentrated weight can loading and rapid pressure tube heating during ballooning, appeared to cause the preferential straining and consequent rupture of the pressure tube between bearing-pad rings. Local heating under the bottom bearing pads did not appear to contribute to pressure tube rupture. In several experiments, the FES contacted the pressure tube between bearing pad locations during ballooning. This caused local thinning of the pressure tube wall in a few tests without causing pressure tube failure. The FES contact with the pressure tube is suspected to be the major contributor to pressure tube rupture in Test 12.

SIMULATION OF THE BEARING PAD EXPERIMENT

The contact conductance between two conforming surfaces depends upon the thermal and physical characteristics of the contacting surfaces and the surrounding environment. The rate of heat transfer across the two contacting surfaces is determined by the thermal contact conductance and the temperature difference between the two surfaces. The thermal contact conductance h_{cc} per unit area of an interface of area A, across which a temperature drop δT exists, is defined by Equation 1:

$$h_{cc} = Q / (A\,\delta T) \qquad (1)$$

where Q is the total rate of heat flow. The temperature difference (δT) is the calculated temperature difference between the two contacting surfaces. Since the relative positions of the two contacting surfaces do not change, δT is generally considered proportional to heat flux Q/A and the constant of proportionality is the conductance coefficient h_{cc}. In several engineering applications, the contact conductance h_{cc} may not be a constant. The experimental evidence from the integrated BP/PT interaction experiments shows that the conductance between bearing pad and the pressure tube may be nonlinear.

The integrated BP/PT interaction experiments were simulated with the objective of deriving the contact conductance between the BP and the PT. The simulations were performed in two steps:

1. The experimental power and pressure transients were input to the SMARTT code to derive the coolant, intermediate and outer ring sheath temperature transients. The sheath-to-coolant and pressure tube-to-coolant heat transfer coefficient transients were also derived. The SMARTT code has been validated against all available PT-DT experiments.

2. The derived transients from step 1 were input to the MINI-SMARTT code to derive the contact conductance between the BP/PT contact. The contact conductance was derived by matching the experimentally measured pressure tube temperature transient as closely as possible. This was achieved by varying the contact conductance as the pressure tube heats up and strains away from the bearing pad.

Since both the SMARTT and MINI-SMARTT computer codes are used in this analysis, a brief overview of both codes is presented along with the modifications and assumptions necessary to simulate these experiments.

SMARTT CODE - DESCRIPTION, MODIFICATIONS, AND ASSUMPTIONS

The SMARTT computer code [1] uses a 2-dimensional, half-bundle model to simulate the temperature response of a CANDU fuel bundle and pressure tube under different scenarios of small and large break loss-of-coolant accidents (LOCAs). Symmetry is assumed across the vertical diameter of the bundle and the assumption of no axial conduction is made. The type of bundle, whether 28 or 37 element, is selected as input to the code as is the type of coolant in the channel. The types of coolant which can be simulated are D_2O, H_2O, and 75%Ar-25%O_2 (simulated steam).

SMARTT uses a finite difference technique to solve for the temperature distribution in each of the fuel elements within the fuel bundle and in the pressure tube. Each fuel element is modelled with 8 angular nodes each of which has 6 radial nodes. The pressure tube is represented with 32 angular nodes each of which has 4 radial nodes. The fuel-element simulators which were used in the experiments were modelled with 4 radial nodes in the graphite core, 1 in the alumina insulator, and 1 in the Zircaloy sheath. The density, thermal conductivity, and specific heat of the respective materials were used in the temperature and heat transfer calculations within each node. Figure 4 and Figure 5 show the details of the fuel-element simulator and the SMARTT nodalization for a 28 fuel element bundle, respectively.

The power, pressure, and saturation steam temperature transients for a simulation are input to the code. When the time step in the calculation is smaller than the interval between input transient values, the code performs a linear interpolation between the input values. The power generation within the graphite heater was assumed to be uniform across the diameter of each graphite rod. The power distribution between the three rings of fuel-elements is set by input parameters. For the simulation of the Bearing Pad Experiments the fuel elements in the inner and middle fuel-element rings were not powered; all of the input power was directed to the 16 elements in the outer fuel-element ring. Temperature, heat transfer, and strain are calculated within the pressure tube model. Pressure tube strain is calculated with the creep strain model for Zr-2.5Nb pressure tubes [3,4]. The heat transfer coefficients between the fuel-element sheaths and the coolant were calculated with Equation 2.

$$HTC_{Sh} = N_{us} * k / D_{hyd} \qquad (2)$$

where N_{us} is the Nusselt number for the coolant, k is the thermal conductivity of the coolant, and D_{hyd} is the hydraulic diameter of the subchannel. A Nusselt number of 4.0, which corresponds to laminar flow, was assumed for all of the analysis. The heat transfer coefficients between the pressure tube and the coolant are set equal to HTC_{Sh} for the subchannel on which the pressure tube node borders.

Radiation between the fuel elements and the pressure tube is treated as diffusely scattered between the surface nodes.

In a 37-element bundle there are 186 surface nodes (150 on the fuel elements and 36 on the pressure tube); for a 28-element bundle there are 144 surface nodes (112 on the fuel elements and 32 pressure tube). A 144x144 radiation view factor matrix accounts for the geometric effects within a non-deformed bundle. Radiation between the pressure tube and calandria tube is treated as occurring between concentric cylinders with an emissivity of 0.3 for the calandria tube. The emissivities of the pressure tube and the fuel-element sheaths were varied for the simulations. The calandria tube is assumed to be at a constant temperature, equal to the moderator temperature, throughout the transient. The Zircaloy/steam reaction is modelled with the reaction rate equations of Urbanic and Heidrick [5].

Several special modifications were implemented in SMARTT to better model the particular bundle geometry of the Bearing Pad Experiments. Figure 2 shows a schematic diagram of the cross-section of the bundle which was used in the experiments. The heat capacity of the fuel elements in the inner and middle fuel-element rings was increased to approximate that of the tungsten-filled can at the centre of the bundle. Equation 3 gives the algorithm used for this purpose.

$$C_p = (2350 + 0.494 * T)\, f_A \quad kJ/(m^3\, K), \qquad \text{if } T < 700\ °C \tag{3a}$$

$$= 2696 * f_A \quad kJ/(m^3\, K), \qquad \text{if } T \geq 700\ °C \tag{3b}$$

where T is the temperature of the fuel-element node and f_A is a correction factor to account for the difference in cross-sectional area between the can and the fuel elements.

SMARTT has been extensively validated against the Pressure-Tube-Delta-T (PTDT) Experiments which were conducted by AECL-WRL. The pressure tube and type of fuel-element simulator which were used in the Bearing Pad Experiments were similar to those used in the supplementary experiments in the Boil-off Series of the PTDT Experiments [8,10,11].

MINI-SMARTT CODE - DESCRIPTION, MODIFICATIONS, AND ASSUMPTIONS

The MINI-SMARTT computer code [2], which was derived from the SMARTT code [1], is used to simulate fuel element and pressure tube response when direct contact occurs between the two components. MINI-SMARTT uses the same solution technique as SMARTT to solve for the temperature distribution in the contacting fuel elements and pressure tube. The thermal-hydraulic conditions and temperatures of the non-contacting fuel elements are input boundary conditions to the code. As in SMARTT, MINI-SMARTT assumes symmetry across the vertical diameter of the pressure tube and no axial conduction. However, there are significant differences in the nodalization scheme and radiation heat transfer model between the two codes.

A finer, graded nodalization scheme is used in both the contacting fuel elements and the pressure tube. Typically 22 radial nodes are used in each fuel element: 18 in the main body of the fuel element and 4 in the bearing pad, when it is present. Ten radial nodes are used in the pressure tube. The angular nodes are varied in size in the contact region in order to match those of the pressure tube and the contacting surface of the fuel element, as well as to obtain a more accurate solution for the temperature distribution in this region. Figure 6 shows schematic diagram of the bearing pad and pressure-tube nodalization in the contact region (the number of nodes has been reduced for clarity). The bearing pads are modelled as extensions of the fuel element.

The following time-dependent, thermal-hydraulic conditions are input to MINI-SMARTT: the coolant temperature, the heat transfer coefficient between the fuel-element sheath and the coolant, and the heat transfer coefficient between the pressure tube and the coolant. These act as boundary conditions within the model and may be calculated with a code such as SMARTT. MINI-SMARTT performs a linear interpolation between the input transient values as required.

Radiation heat exchange between the fuel-element rings and between the outer fuel-element ring and the pressure tube is modelled as occurring between concentric cylinders (Equation 4).

$$q_{rad} = \varepsilon_1 \varepsilon_2 \sigma (T_1^4 - T_2^4) / \{\varepsilon_2 + \varepsilon_1 (A_1/A_2) (1 - \varepsilon_2)\} \quad (4)$$

where q_{rad} is the radiant flux from surface 1 to surface 2; σ is the Stefan-Boltzmann constant; ε_1 and ε_2 are the emissivities of surfaces 1 and 2, respectively; A_1 and A_2 are the areas of surfaces 1 and 2; and T_1 and T_2 are the temperatures of the two surfaces. The temperature transients for the middle and outer fuel-element rings are input to MINI-SMARTT which performs a linear interpolation between the input values as required. A detailed temperature calculation is performed, however, for each contacting fuel element. Radiation from the contacting fuel elements is accounted for in the solution of the temperature distribution in the fuel element by dividing the total radiant energy from the fuel ring by the number of fuel elements in the ring and assigning this fraction to each contacting fuel element. The fuel element is divided in half with the contribution to the total radiant energy from the radiant exchange between the fuel-element ring and the pressure tube assigned to the outward-facing half of the fuel element. The contribution from radiant exchange between the middle and outer fuel-element rings is assigned to the inward-facing half of the fuel element. The radiant energy is distributed to each surface node of the fuel element with the use of normalized view factors. The view factors for each half (inward-facing and outward-facing halves) of the fuel element are independently normalized (Equation 5).

$$Q_{radFEi} = Q_{radORPT} f_{VFi} / (N_{OR} a_i r_i) , \qquad \sum_i f_{VFi} = 1 \quad (5)$$

where Q_{radFEi} is the radiant flux from outward-facing surface node i of a contacting fuel element, $Q_{radORPT}$ is the total radiant power per unit length from the outer fuel-element ring to the pressure tube, f_{VFi} is the view factor for node i, a_i and r_i are the angular extent and outer radius of fuel element node i, and N_{OR} is the number of elements in outer fuel-element ring. The total radiant power per unit length from the outer fuel-element ring to the pressure tube is given by Equation 6.

$$Q_{radORPT} = \sum_j q_{radPTj} a_j r_{PT} \quad (6)$$

where q_{radPTj} is the radiant flux incident on pressure tube node j, a_j is the angular extent of node j in radians and r_{PT} is the inner radius of the pressure tube. Radiation between the pressure tube and calandria tube is also modelled as occurring between concentric cylinders as it is in SMARTT.

As in SMARTT the thermal conductivity of the various materials in the fuel element are used in the calculation of the temperature distribution within the element. However, MINI-SMARTT also accounts for the conductivity of ZrO_2 in the contact region. As the fuel element oxidizes heat conduction through the fuel element to the contact zone is increasingly slowed due to the lower thermal conductivity of the ZrO_2 relative to that of Zircaloy. The rate of formation of ZrO_2 is modelled with the equations of Urbanic and Heidrick [5]. Both fuel-element and pressure-tube surfaces are considered. On the bearing pad the reaction front is tracked and the energy from the reaction is added to the node that contains the front.

The algorithm which is used to calculate pressure tube strain in MINI-SMARTT is the same as in SMARTT with the exception that a spline fit is performed to obtain a better estimate of the strain in the contact region. The pressure tube is assumed to have ballooned into contact with the calandria tube if the average pressure tube strain reaches 18.0% and to have failed if the local true strain reaches 100%, which is equivalent to 37% of the original thickness of the pressure tube, before PT/CT contact occurs.

MINI-SMARTT was modified to permit contact of any number of fuel elements at specified locations on the pressure tube within the half-bundle model. The nodalizations of each contacting fuel element and contact location on the pressure tube are input separately; the code, however, checks for any conflicts in the chosen nodalization schemes.

The option of using a time-varying contact-heat-transfer coefficient was added to the code. MINI-SMARTT reads the input transient values and performs a linear interpolation between them when the transient time step is larger than that used in the temperature calculations. When multiple fuel elements are in contact with the pressure tube, the contact-heat-transfer coefficient can be weighted to reflect differences in the degree of contact at each location. The contact heat flux between contacting surface-node j of the fuel element and node i of the pressure tube is given by Equation 7.

$$q_{conj} = H_{con} (T_{FEj} - T_{PTi}) \quad (7)$$

where H_{con} is the contact heat transfer coefficient, T_{FE_j} is the temperature of node j of the fuel element, and T_{PTi} is the temperature of node i of the pressure tube. Contact between the bearing pad (or fuel element) and the pressure tube is assumed to be uniform over the contact region (e.g. the surface of the bearing pad).

PREDICTION OF EXPERIMENTAL RESULTS USING THE SMARTT AND MINI-SMARTT CODES

The SMARTT code was used to simulate the thermalhydraulic transient conditions which were used as input to the MINI-SMARTT code. The measured power and pressure transients for a test as well as the initial coolant and pressure-tube temperatures were input to SMARTT code. Light water coolant properties were used in the simulation of the experiments in phase 1. Simulated steam, 75%Ar-25%O_2, coolant properties were used in the simulation of the experiments in phase 2. The fuel-sheath and pressure-tube emissivities were adjusted in the SMARTT simulation to give the best fit to the experimentally measured temperatures of the fuel-element sheath and pressure tube at an axial location in the test section where there was no bearing pad contact, *e.g.* an axial location equidistant between bearing pad rings. Emphasis was placed on the fit to the pressure-tube temperature transient in selecting the "best fit" simulation.

The detailed simulation results are shown for three experiments, namely, experiment 3 of phase 1 and experiments 8 and 12 of phase 2. Experiment 3 was conducted in a steam environment at system pressure of 6 MPa. A "worn" bearing pad was used in experiment 8 with system pressure of 3 MPa. A worn bearing pad was defined as a bearing pad that was abraded on its bearing surface. Experiment 12 was performed at system pressure of 3 MPa with fuel element simulator power slightly higher than experiments 3 and 8 (10 kW/m for experiment 12 vs. 8.3 kW/m and 8.5 kW/m for experiments 3 and 8, respectively). The pressure tube ruptured in experiment 12 between bearing pad rings due to FE/PT contact. Both experiments 8 and 12 were conducted in simulated steam environment (75% Ar - 25% O_2).

A comparison of the SMARTT predictions and experimental measurements for the outer fuel-element-sheath temperatures is shown in Figure 7 for Test 12. This comparison shows that the SMARTT code, given the experimental boundary conditions, can produce the outer ring sheath temperature transient. Figure 8 shows comparison of the measured pressure tube temperatures between bearing pad locations and predicted pressure tube temperatures by the SMARTT and MINI-SMARTT codes. The pressure tube temperature transient is well predicted by both codes between bearing pad locations.

Initially, MINI-SMARTT was used to simulate the experiments with a single bearing pad contacting at the bottom of the pressure tube. However, the measured circumferential temperature profiles on the pressure tube suggested that more than one bearing pad was in contact with the pressure tube at the same time. This was supported by the observation of indentations on the inside surface of the pressure tube due to bearing pads. The number of contacting bearing pads was determined for each experiment from the circumferential temperature profiles and used in MINI-SMARTT code simulations of the experiment.

To best fit the measured pressure-tube temperatures, the contact-heat-transfer coefficient, H_{con}, was varied during the transient. Values of H_{con} for the best fit to Tests 3, 8 and 12 experimental measurements are given in Table 3. Note, however, that the simulated pressure-tube temperature is not sensitive to the value of H_{con} when the bundle power

is low.

Comparison of the simulated and experimental pressure tube temperatures are given in Figure 9 for Test 3. Figure 10 shows a similar comparison for the temperatures of the bottom bearing pad and fuel element sheath. Figure 9 shows that the pressure tube temperature at the bottom was fitted well by changing the contact conductance. The pressure tube temperature at circumferential location 22.5° anti-clockwise from the bottom of the pressure tube was slightly under predicted. The comparison between MINI-SMARTT code predictions and the bottom bearing pad and fuel element sheath shown in Figure 10 indicates that the fuel element sheath temperature is well predicted by the code; however, the bearing pad temperature was overpredicted. This experiment was conducted in a steam environment and some condensation was observed at the bottom of the bearing pad for all the experiment in this series. The presence of condensation would contribute to cooling the bearing pad and explain the code overprediction of bearing pad temperatures.

It should be noticed that the change in bearing pad and pressure tube heatup rates, observed in Figures 9 and 10, at about 127 seconds into the transient coincided with the rupture in a tungsten weight can positioned inside the fuel element simulator bundle. This rupture was caused by thermal expansion of the gas inside the weight can during heatup. The extra force acting on the bearing pad from this pressurized (ballooning) weight can could potentially cause changes in the contact conductance between the bearing pad and the pressure tube. This is reflected in the value of the contact conductance required to fit the pressure tube temperature; the contact conductance increased to 1 kW/m^2K as indicated in Table 3.

The decrease in the contact conductance later in the transient is due to bulging (local straining) of the pressure tube away from the bearing pad contact and eventually the pressure tube balloons into contact with the calandria tube. This phenomenon was observed in Test 6 where the pressure tube ruptured before contacting the calandria tube due to high top-to-bottom differential circumferential temperature. Once the pressure tube balloons into contact with the calandria tube, the local bulges are flattened and conformed to the inside surface of the calandria tube.

A similar procedure was followed to best fit the measured pressure tube temperatures at the assumed contact points for Tests 8 and 12. The contact heat transfer coefficient, H_{con}, was varied during the transient. Values of H_{con} for the best fit to Tests 8 and 12 are given in Table 3. Comparison of the simulated and experimental pressure tube temperatures are given in Figure 11 for Test 8. Figure 12 shows a similar comparison for the temperatures of the bottom bearing pad and fuel element sheath for this test. Figures 13 and 14 show pressure tube, bearing pad and fuel element temperature comparisons, respectively, for Test 12.

Test 8 used a "worn" bearing pad which conformed better to the inside surface of the pressure tube than "as-received" bearing pad and, hence, established good solid-to-solid contact at the interface of the contact area. This is reflected in the high contact conductance required to reproduce the measured pressure tube temperatures in this test. The highest contact conductance in all of the experimental series was obtained from Test 8. Table 3 shows that a high contact conductance of 1.6 $kW/m^{2o}K$ was required in Test 8 for the best fit of the measured pressure tube temperatures. A good comparison of the measured and predicted pressure tube temperatures is shown in Figure 11. The agreement between measured and predicted fuel element sheath and bearing pad temperatures shown in Figure 12 is reasonable.

In general, supporting experimental evidence showed that the experimental data indicated that bearing-pad-to-pressure- tube contact conductance did not remain constant during heating of the fuel bundle. Instead, it increased significantly until a threshold temperature was reached and then decreased once the pressure tube began to balloon. Strain related local deformations (bulging) influenced the thermal interactions of the bearing pad and the pressure tube. The decrease in pressure tube heatup rate was attributed to a pressure tube bulge along the axial direction opposite the bearing pad. This bulge allowed the pressure tube to deform away from the bearing pad and, hence, decrease the contact conductance (Table 3). The heating rate of the bearing pad increases as it loses contact with the pressure tube (Figure 12) which generally coincide with decrease in the pressure tube heating rate.

Test 12, which used an "as-received" bearing pad, required a significantly lower peak contact conductance in the MINI-SMARTT simulation than did Test 8. This is attributed to the poorer conformity of the "as-received" bearing pad to the pressure tube than occur for worn bearing pad. The MINI-SMARTT simulation of the pressure tube temperatures at the bottom and 22.5° locations agree well with the measured values while a slight underprediction is shown at 45° location (Figure 13). The comparison between the predicted and measured fuel element sheath and bearing pad temperatures is shown in Figure 14. The MINI-SMARTT predictions overpredict the experimental measurements (Figure 14).

GENERAL DISCUSSION

In all the bearing pad/pressure tube contact experiments, the pressure tube ballooned into contact with the calandria tube with the exception of three experiments. In experiments 6 and 10, the pressure tube ruptured due to a large circumferential temperature difference induced by the experimental procedure. The system pressure in both experiments 6 and 10 was high at 6 MPa. The pressure tube is expected to fail at this high internal pressure with a large circumferential temperature difference and sharp gradient from top-to-bottom. This is demonstrated by the pressure tube/calandria tube contact heat transfer experimental results where four experiments were carried out at 6 MPa. In two of the experiments, the pressure tube ballooned into contact with the calandria tube and the maximum top-to-bottom temperature differentials were less than 100°C. In the other two experiments, the pressure tube ruptured before contacting the calandria tube. The maximum top-to-bottom temperatures differential were greater than 100°C (refer to Reference 12).

In experiment 6, free convection current enhanced by the initial differential temperature on the pressure tube circumference (bottom 40°C hotter than top) caused a top-to-bottom circumferential temperature gradient of 135°C during the heatup phase. The pressure tube ruptured at the top as a result of excess strain along the top of the pressure tube prior to contact with the calandria tube (refer to Reference 13).

Experiment 10 was performed with the high pressure and power conditions used in experiment 6. A temperature gradient (bottom was 120°C hotter than the top) was imposed on the pressure tube during the pretest warm-up stage to counteract the preferential convection heating that was believed to be the cause for pressure tube failure in experiment 6. This bottom-to-top temperature gradient, in combination with the high test-section pressure (6 MPa), caused the pressure tube to preferentially strain and rupture along the bottom during the ballooning phase. Prior to rupture, the bottom of the pressure tube was 185°C hotter than the top at the central bearing pad ring and 225°C hotter on the bottom than on the top between bearing pad rings.

The third pressure tube failure occurred in experiment 12. The reason for failure was attributed to a fuel element contacting the pressure tube between the bearing pad rings. The pressure tube was ballooning and straining away from the bearing pad when the fuel element came into contact with the pressure tube causing a localized hotspot which led to localized thinning of the pressure tube wall and eventually rupturing the pressure tube.

The post test examination showed graphite/alumina interaction was evident at several locations where the graphite was bonded to the alumina. Also, several alumina insulators were darkened along the interface between the insulators. This interaction and overall appearance suggested the fuel element simulators had nearly reached the high temperature and high circuit voltage required to cause electrical arc and failure of the heaters before full PT/CT contact. However, arcing was ruled out as the cause of pressure tube failure. In addition, thermocouple wires between the pressure tube and the calandria tube may have contributed to pressure tube failure by interfering with PT/CT contact. Due to these uncertainties encountered in experiment 12, the outcome of this experiment should not be considered as a typical outcome of BP/PT interaction.

One of the differences between the experimental setup and the reactor case is that the weight of the tungsten cans is concentrated on the outer ring of the fuel elements while the weight of the bundle in the reactor case is distributed over all the elements. Also the fuel element simulators do not have the freedom to bow to the inside of the bundle due to the differential temperature developed on the fuel element (inside surface facing other elements is hotter than

outside surface facing the pressure tube, i.e. bowing away from the pressure tube).

In most of the bearing pad experiments, evidence showed that the fuel element contacted the pressure tube between bearing pad rings. Some of these contacts caused a slight thinning of the pressure tube wall but only Test 12 caused pressure tube failure. The only difference in Test 12 is the relatively high pressure tube heating rate of 10°C/s as compared to 9°C/s in Test 9. The pressure tube ballooned and contacted the calandria tube at the bottom centreline bearing pad and was close to contact at the top and between bearing pad locations when the rupture occurred.

CONCLUSIONS

1. The bearing pad/pressure tube experiments have been analyzed and simulated to derive the contact conductance between contacting bearing pad and pressure tube. The SMARTT code was used to derive the transient thermalhydraulic boundary conditions which were used as input to the MINI-SMARTT code. A best fit approach was used to predict the measured pressure tube temperatures. This was done by using transient values of contact conductance as input to the MINI-SMARTT code. The MINI-SMARTT code was modified to be able to simulate multiple bearing pad contact on the pressure tube circumference. The derived contact conductances are small enough to ensure fuel channel integrity (FCI) when single or multiple bearing pad contact occurs.

2. The largest contact conductance was found to be 1.6 kW/m^2K in Test 8 (worn bearing pad). This value is recommended to be used in the analysis of bearing pad/pressure tube interaction.

3. The pressure tube rupture in experiments 6 and 10 was due to a large top-to-bottom temperature differential which was an artifact of the experimental procedure. This conclusion is supported by the pressure tube/calandria tube contact heat transfer experimental results.

4. Experiment 12 should not be considered as a typical outcome of BP/PT interaction due to the uncertainties encountered in this experiment.

REFERENCES

[1] LOCKE K.E. et al, "SMARTT - A Computer Code to Predict Fuel and Pressure Tube Temperature Gradient Under Asymmetric Coolant Conditions", Proc. 6th Annual CNS Conference, Ottawa, June 1985.

[2] REEVES D.B. et al, "Development of MINI-SMARTT Code for Fuel Element/Pressure Tube Contact", Proc. 2nd Int. Conf. (CNS) on Simulation Methods in Nuclear Engineering, Montreal, October 1986.

[3] ARCHINOFF G.H. and KUNDURPI P.S., "Pressure Tube Integrity During Ballooning with a Non-Uniform Circumferential Temperature Gradient", OH-DD-84433, November 1984.

[4] SHEWFELT R.S.W. and GODIN D.P., "Ballooning of Thin-Walled Tubes with Circumferential Temperature Variations", AECL-8317.

[5] URBANIC V.F. and HEIDRICK T.R., "High-temperature Oxidation of Zircaloy-2 and Zircaloy-4 in Steam", Journal of Nuclear Materials, 75, 251-261, 1978.

[6] LOCKE K.E., LUXAT J.C., MUZUMDAR A.P., SO C.B., MOYER R.G., and LITKE D., "Progress on SMARTT simulation of pressure tube circumferential temperature distribution experiments - Test 1 to 4", Conference of the Canadian Nuclear Society, St. John, New Brunswick, June 1987.

[7] BAYOUMI M.H., MUIR W.C., and KUNDURPI P.S., "Further simulation of the pressure tube circumferential temperature distribution experiments (Make-up water series)", Proceedings of the 13th Annual Conference of the Canadian Nuclear Society, St. John, New Brunswick, June 1992.

[8] BAYOUMI M.H., MUIR W.C., and KUNDURPI P.S., "Simulation of the pressure tube circumferential temperature distribution experiments (Boil-off experiments)", Proceedings of the 4th International Conference on Simulation Methods in Nuclear Engineering, Montreal, June 1993.

[9] BAYOUMI M.H., MUIR W.C., and KUNDURPI P.S., "Simulation of the pressure tube circumferential temperature distribution experiments (Variable make-up water series)", INC93: International Nuclear Congress and Exhibition, Toronto, October 1993.

[10] BAYOUMI M.H., MUIR W.C., and KUNDURPI P.S., "Simulation and investigation of the pressure tube circumferential temperature distribution experiments (Boil-off Series of Experiments)", 14th Conference of the Canadian Nuclear Society, Montreal, June 1994.

[11] MUIR W.C. and BAYOUMI M.H.,"Simulation and Analysis of the Thermal and Deformation Behaviour of "As-Received" and "Hydrided" Pressure Tubes Used in the Circumferential Temperature Distribution Experiments (End of Life/Pressure Tube Behaviour), 15th Conference of the Canadian Nuclear Society, Saskatoon, June 1995.

[12] MOYER R.G. and GILLESPIE G.E., "Pressure-Tube/Calandria-Tube Contact Heat Transfer Experimental Data", Atomic Energy of Canada Limited, Whiteshell Laboratories, Report No. CANDEV-86-95, December 1986.

[13] MOYER R.G. et al."Bearing -Pad/Pressure-Tube Rupture Experimental Summary Report for Series @, Tests 5-12", Atomic Energy of Canada Limited, Whiteshell Laboratories, Report No. COG-94-252, November 1994.

Table 1
Experimental Conditions of Test 1 to 4

Test No.	Coolant Pressure (MPa)	FES Power (kW/m)	Moderator Subcooling (°C)
1	2 - 3	4.1	24
2	3 - 3.5	8.3	25
3	6	5.0	25
4	6	8.4	25

Table 2
Experimental Conditions of Test 5 to 12

Test No.	Coolant Pressure (MPa)	Bundle Power (kW/m)	FES Power (kW/m)	Moderator Subcooling (°C)
5	3	130	8.1	25
6	6	123	7.7	26
7	3	130	8.1	25
8	3	136	8.5	24
9	3	128	8.0	25
10	6	130	8.1	26
11	1	131	8.2	26
12	3	162	10.1	25.5

Table 3
Best-Fit Contact Heat Transfer Coefficient Transients for Multi-Pin Contact MINI-SMARTT Simulations

Test 3		Test 8		Test 12	
Time (s)	Hcon (kW/(m² K))	Time (s)	Hcon (kW/(m² K))	Time (s)	Hcon (kW/(m² K))
0	0.60	0	0.20	0	0.20
51	0.60	45	0.20	20	0.25
75	0.65	46	0.30	49	0.25
80	0.70	100	0.30	50	0.30
81	0.90	101	0.35	84	0.40
105	1.00	149	0.35	85	0.55
129	1.00	150	0.40	95	0.65
130	0.50	175	0.50	2000	0.65
140	0.00	180	0.60		
2000	0.00	190	0.60		
		191	0.80		
		210	1.00		
		211	1.50		
		227.5	1.50		
		229.5	1.60		
		230	0.70		
		2000	0.10		

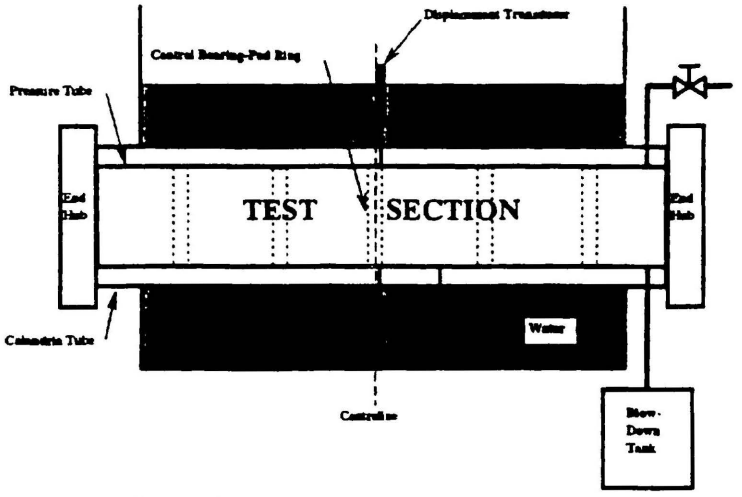

Figure 1: Schematic diagram of experimental apparatus.

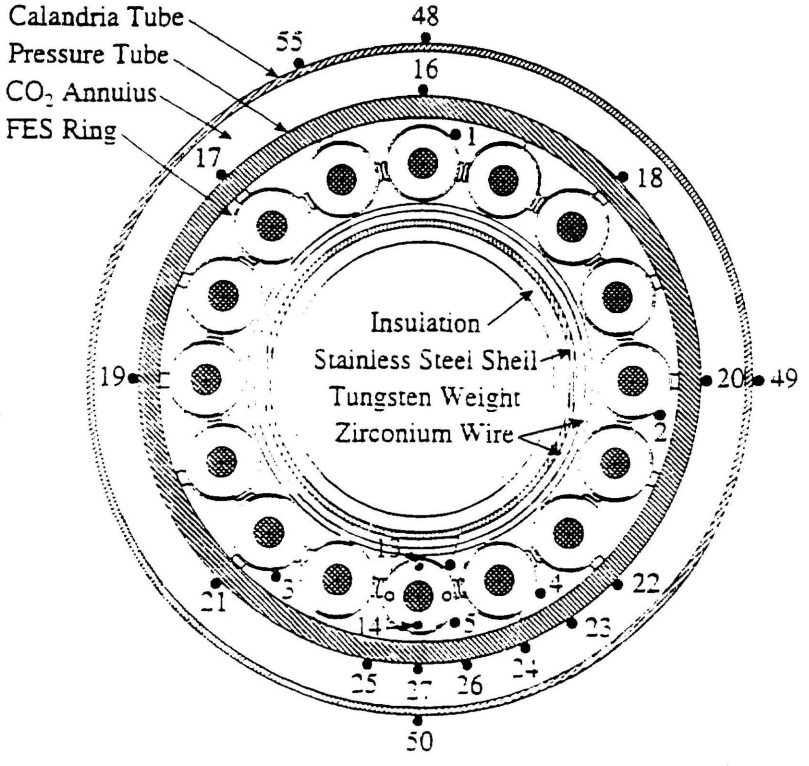

Figure 2: Typical locations of thermocouples at the Test Section centreline.

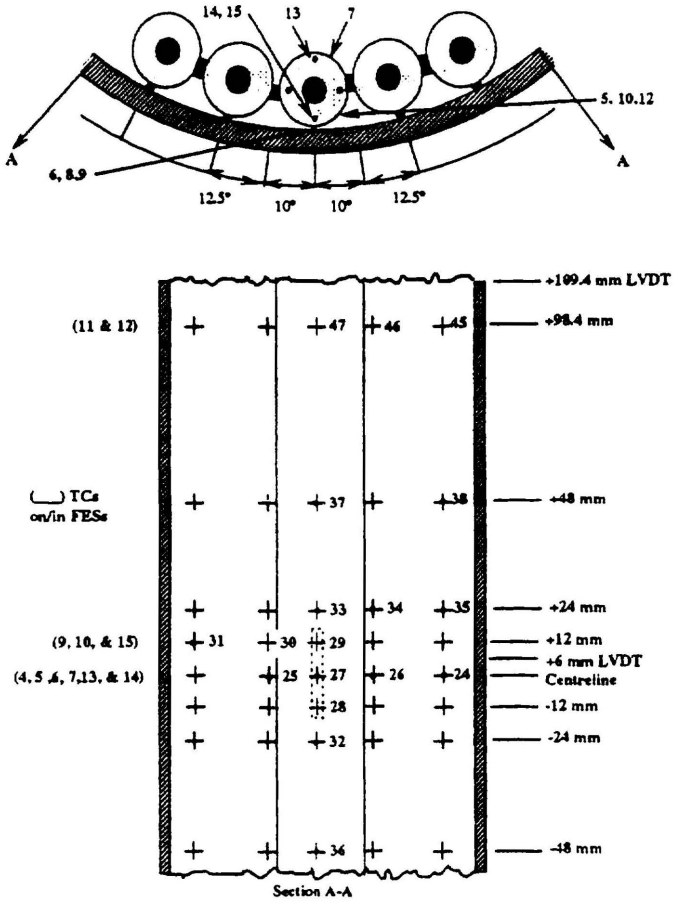

Figure 3: Typical thermocouple grid and displacement transducer (LVDT) locations on the bottom of the pressure tube.

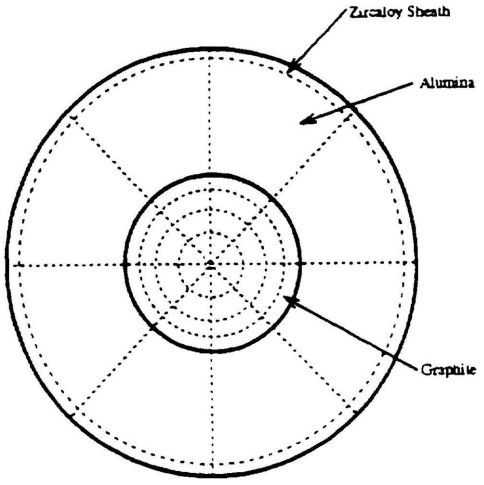

Figure 4: Schematic diagram of fuel-element simulator with SMARTT nodalization.

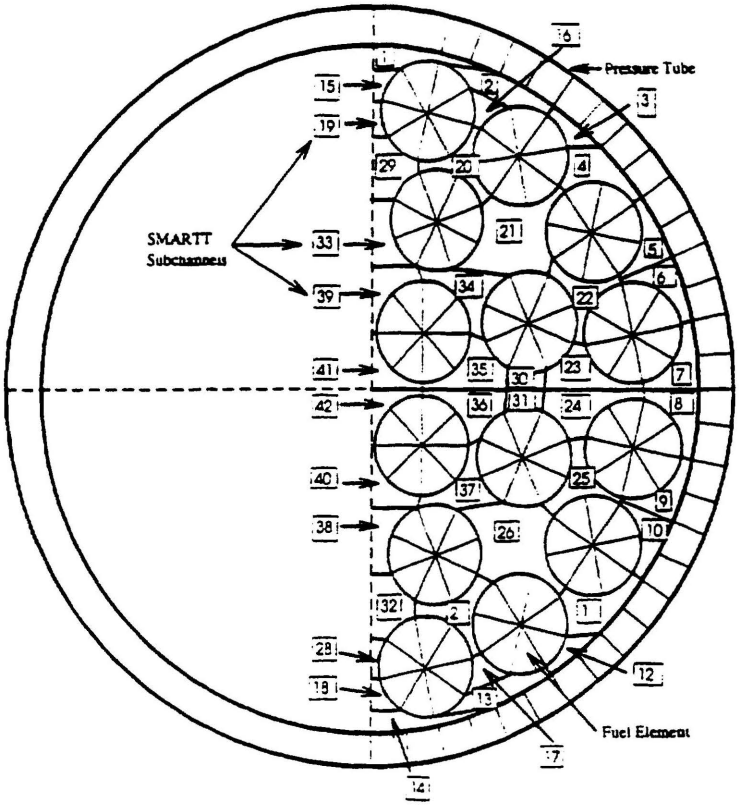

Figure 5: Schematic diagram of 28-element bundle showing subchannel nodalization in SMARTT.

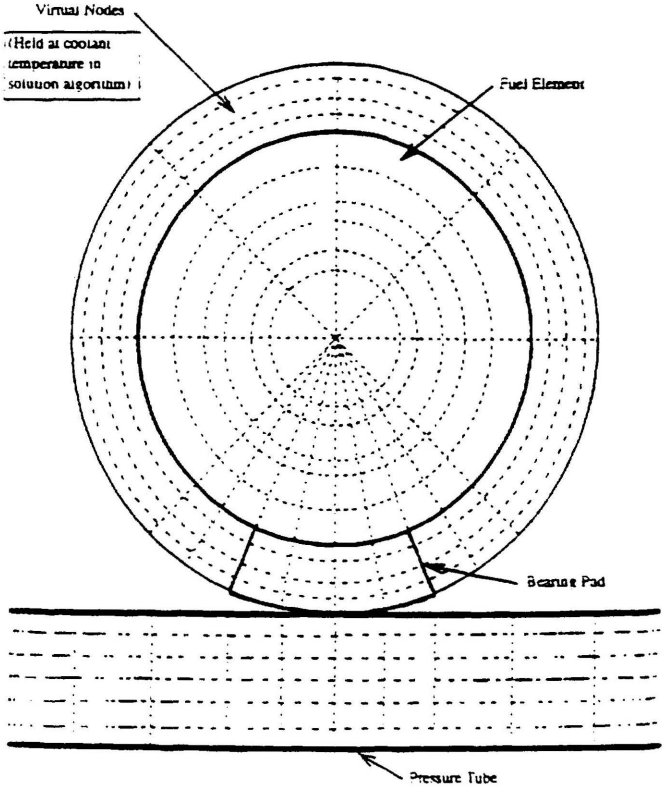

Figure 6: Schematic diagram of fuel-element, regular-bearing-pad, and pressure-tube nodalizations in MINI-SMARTT.

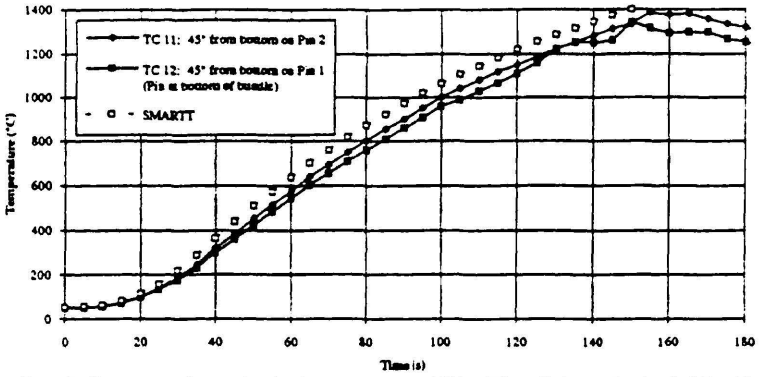

Figure 7: Comparison of outer ring sheath temperatures and SMARTT prediction for Bearing Pad Test 12 at the non-contact ring.

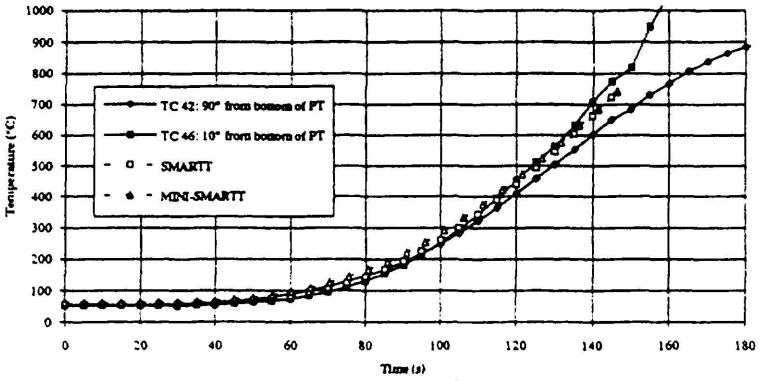

Figure 8: Comparison of pressure tube temperatures and SMARTT and MINI-SMARTT predictions for Bearing Pad Test 12 at a non-contact ring.

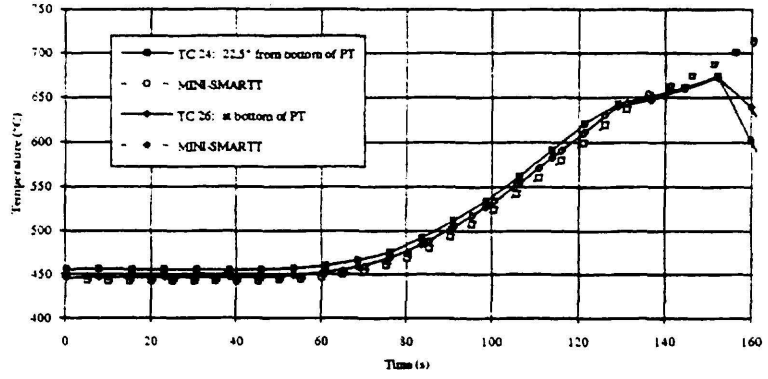

Figure 9: Pressure tube temperatures measured and predicted by MINI-SMARTT for Bearing Pad Test 3.

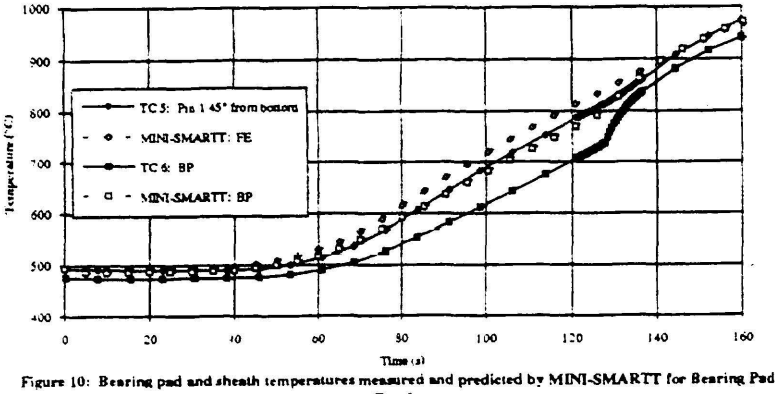

Figure 10: Bearing pad and sheath temperatures measured and predicted by MINI-SMARTT for Bearing Pad Test 3.

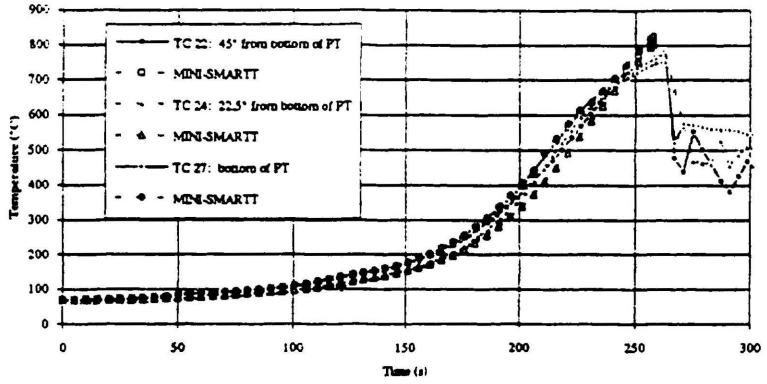

Figure 11: Pressure tube temperatures measured and predicted by MINI-SMARTT for Bearing Pad Test 8.

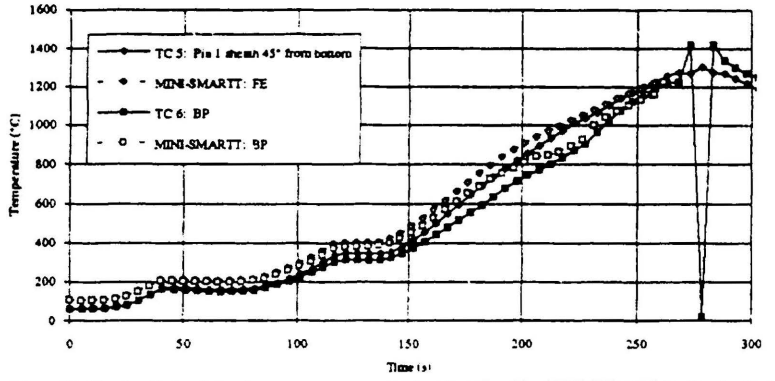

Figure 12: Bearing Pad and sheath temperatures measured and predicted by MINI-SMARTT for Bearing Pad Test 8.

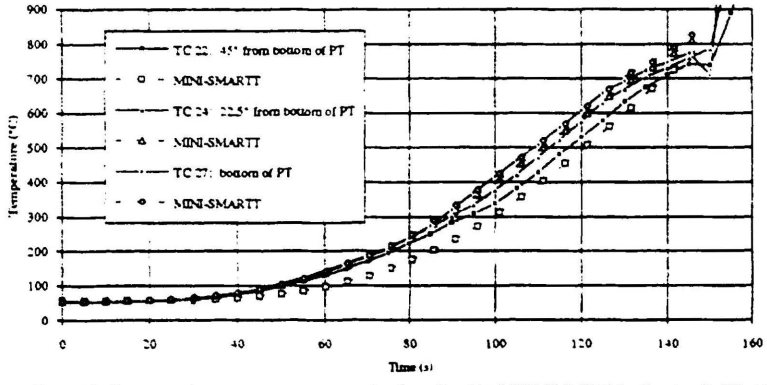

Figure 13: Pressure tube temperatures measured and predicted by MINI-SMARTT for Bearing Pad Test 12.

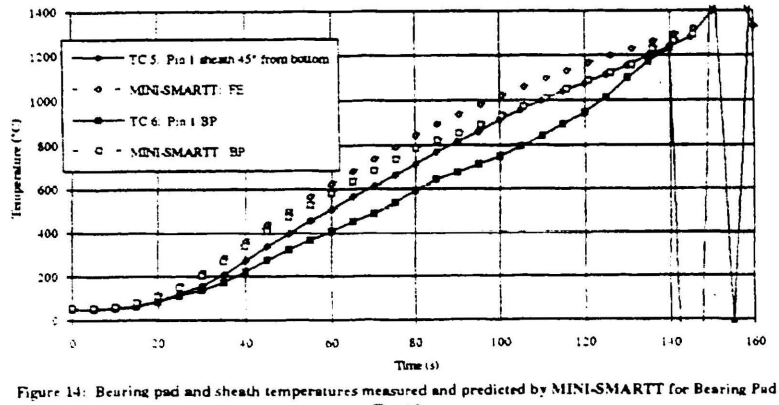

Figure 14: Bearing pad and sheath temperatures measured and predicted by MINI-SMARTT for Bearing Pad Test 12.